3. SUPPLEMENTARY FIGURE LEGENDS

Fig. S1. CRISPR/Cas9- and PhiC31-mediated genome editing for expression from endogenous loci. (A) Site-specific insertion of an *attP* landing site into the *ptc* locus (to generate *ptc[KO; attP, pax-Cherry]),* using CRISPR/Cas9-mediated homologous recombination (see Methods). The red fluorescence of *pax-Cherry* served to identify candidates and can be used to track the allele. (B) PhiC31 integrase-mediated integration of DNA fragments in the *attP* site. Here, mini *white* (red eyes) was used to select candidates. Insert not drawn to scale.

Fig. S2. GFP can diffuse in and out of imaginal discs. (A) Schematic representation of the paths a diffusing protein can take following secretion (diffusion through the basolateral space and exchange with the hemolymph). The fat body is a large adipose tissue with extensive contact with the hemolymph. (B) Diffusion out of imaginal discs (*in vivo*). Western blot of hemolymph and wing discs collected from larvae expressing *UAS-SecGFP* under the control of *vg-Gal4* (active only in wing/haltere primordia). The presence of GFP in the hemolymph shows that GFP can cross the basal lamina and leak out of the disc. (C) Diffusion into imaginal discs (*in vivo*). SecGFP produced by the fat body (*lpp-Gal4, UAS-SecGFP*) was captured by imaginal discs expressing *LexAop-Nb1^{high}CD8* under the control of *dpp-LHG*. (D) Diffusion into imaginal discs (*ex vivo*). Imaginal discs expressing *UAS-Nb1^{high}CD8* under the control of *dpp-Gal4* were bathed in GFP conditioned medium for 30 min at room temperature and washed before imaging. Note the accumulation of GFP at the surface of *dpp*-expressing cells. GFP was not found on the apical side, which is separated from the GFP bath by septate junctions. Scale bars: 50 µm.

Fig. S3. Modeling the apical gradient. (A) Nb1^{high}CD8 in the apical (left) and lateral (right) domain of a *ptc-SecGFP, hh-Nb1^{high}CD8* wing disc. **(B)** Measurements of the fluorescent intensity suggest a ~4-fold higher level of Nb1^{high}CD8 in the apical than in the basolateral domain. (**C**) Fluorescence intensity profiles in the apical space for *hh-Nb1^{high}CD8* (n=12) and *hh-Nb1^{high}CD8* + fat-body trap (n=12). The two profiles are largely overlapping, indicating that the apical gradient is unaffected by GFP trapping in the hemolymph. (**D**) Comparison of the apical profiles (dotted lines) with the corresponding basolateral profiles (solid lines; also shown in Fig. 1D) for *hh-Nb1^{high}CD8* (green) and *hh-Nb^{low}CD8* (blue). All profiles are normalized to the GFP fluorescence intensity at the source. GFP levels are generally larger in the apical domain than in the basolateral domain. (**E**) Model prediction for the profiles shown in (D). The model is as for the basolateral gradient but takes into account the absence of leakage, the change in geometry of the intercellular space and an increased receptor density (see section 1.8 in the Supplementary Theory for details). With these modifications, the model captures the main features of the apical gradient.

Fig. S4. Nanobody-mediated fluorescence boosting has a limited impact on model predictions. GFP fluorescence is modulated by binding to nanobodies (*16*). For example, *in vitro*, Nb1^{high} boosts GFP fluorescence by 50%. Here, we investigate the impact of this effect on the model's predictions. Panels (A,C,E) assume equal fluorescence intensity when GFP is bound

to Nb1^{high}*CD8* or Nb^{low}*CD8,* and are plotted using the parameters listed in Table S2. Panels (B,D,F) assume the intensity of GFP is 1.5 larger when bound to Nb1^{high}*CD8* than free or bound to Nb^{low}*CD8*, and are plotted using the parameters fitted to the adjusted GFP intensity profiles $\mathrm{j} = 0.32\ \mathrm{nM.s^{-1}}$, $\kappa = 0.07\ \mathrm{s^{-1}}$, $\bar{k}_H = 0.0052\ \mathrm{s^{-1}}$, $\bar{k}_H^{FB} = 0.15\ \mathrm{s^{-1}}$, $j_r = 0.003\ \mathrm{nM.\mu m.s^{-1}}$. **(A-B)** Bound GFP profiles normalized to the total concentration of receptor (panel A is as in Fig. 2C. The blue and green curves are obtained by using the known on and off rates for the low- and high-affinity receptors respectively; purple curve is obtained by increasing degradation in the hemolymph. **(C-D)** Predicted GFP profile following 20-fold increase in binder expression (orange curve compared to green curve), normalized to the lower value of the total concentration of receptors. Panel C is as in Fig. 3A. **(E-F)** Predicted bound GFP profiles for *ptc-SecGFP, hh-Nb1^{high}CD8* (green curve, as shown in Fig. 2C) and for an increasing rate of SecGFP production j (curves with increasing magenta intensity). Normalization as in Fig. S6A. Panel E is as in Fig. S6A. Profiles are normalized to the total concentration of receptor.

Fig. S5. A diffusion-degradation-leakage gradient model. Parameters are stated in Table S2, unless specified otherwise**. (A)** Schematic of one-dimensional model geometry. The mean intercellular distance is denoted h (upper schematic). The width of the source is denoted L_S, the width of the anterior and posterior compartments L (lower schematic). **(B)** A threshold level of surface density of bound receptors n_b^* determines the boundary of the activation domain (x^*) of a hypothetical downstream target (orange). **(C)** Profiles of bound receptors surface density, for different values of the total receptor surface density, in the absence of ligand in the hemolymph. The effect of receptor saturation is neglected in these plots, allowing for analytical results. Elevating receptor surface density results in an increase of concentration near the source and a reduction of the characteristic length scale. n_b^* (blue dashed line) indicates a hypothetical threshold for target gene activation. $j = 0.05\mathrm{nM.s^{-1}}$, $k = 2.6\times10^{-5}\ \mathrm{s^{-1}}$, $n_\mathrm{T} = 15\mathrm{nM.\mu m}$ (brown), 40 nM.μm (green), 200 nM.μm (red), $c_\mathrm{H} = 0, n_\mathrm{b}^* = 10\mathrm{nM.\mu m}$; other parameters are stated in Table S2. **(D)** On/off target boundary (x^*) as a function of the total receptor surface density, in the absence of receptor saturation and ligands in the hemolymph. The activation threshold ($n_\mathrm{b}^* = 10\mathrm{nM.\mu m}$) in panel C was used to determine x^* for different receptor surface density (dots corresponds to curves with the same color in panel C). A maximal target domain size can be found for intermediate values of the total receptor surface density. **(E)** Profiles of bound receptors surface density, for different values of the total receptor surface density, considering the presence of ligand in the hemolymph. $j = 0.01\ \mathrm{nM.s^{-1}}$, $k = 2.6\times10^{-5}\ \mathrm{s^{-1}}$, $n_\mathrm{T} = 1\mathrm{nM.\mu m}$ (brown), 3 nM.μm (green), 100 nM.μm (red), 800 nM.μm(purple), $\bar{k}_\mathrm{H} = 0.01\ \mathrm{s^{-1}}$, $n_\mathrm{b}^* = 0.7\mathrm{nM.\mu m}$; other parameters are stated in Table S2. **(F)** Phase diagram of target activation domain size, as a function of total receptor surface density and effective ligand degradation rate in the hemolymph. Receptor saturation is not taken into account. At low receptor density level, no activation occurs; at intermediate receptor density and for low enough degradation in the hemolymph, a region of full activation appears (dots correspond to curves with the same color in panel E); the third domain of parameter space is that of biologically relevant spatially restricted activation. Parameters as in panel E. **(G)** Phase

diagram as described for panel F, but with receptor saturation included. Color code corresponds to the size of the activated domain. **(H, I, J, K)** Free ligand concentration (H, J) and effective 3D bound receptor concentration (as opposed to membrane density) in the intercellular space (I, K) profiles for different k_{on} (H, I) and, k_{off} values (J, K). The relative levels of free ligand concentration and effective 3D bound receptor concentration indicate that the GFP fluorescence profile is largely dominated by bound receptors. $n_{\mathrm{T}} = 80\mathrm{nM}.\mu\mathrm{m}$, and other parameters as in Table S2.

Fig. S6. Increasing ligand production extends and flattens the gradient. (A) Bound GFP profile calculated from the diffusion-degradation-leakage model, normalized to the total concentration of receptors. Predicted profiles for parameters given in Table S2 (green curve, as shown in Fig. 2C, corresponding to the *ptc-SecGFP, hh-Nb1^{high}CD8* experiments) and for an increasing rate of secreted GFP production in the source (curves with increasing magenta intensity). The gradient shape changes and flattens as a result of increased binder saturation and GFP entering the tissue from the hemolymph. Other parameters are taken from Table S2. **(B)** Wing disc expressing ligand and binder as in Fig. 1C (*ptc-SecGFP, hh-Nb1^{high}CD8*). **(C)** Increasing SecGFP (*ptc-Gal4, UAS-SecGFP, hh-Nb1^{high}CD8*) lengthens the gradient range and saturates binders up to 40 µm from the source. **(D)** Fluorescence profiles obtained from panels B and C (compare to curves in panel A). Since the source intensity was different in the two experiments, values were not normalized. *ptc-SecGFP, hh-Nb1^{high}CD8,* n=6; *ptc-Gal4, UAS-SecGFP, hh-Nb1^{high}CD8,* n=7. Scale bars: 20 µm.

Fig. S7. Experimental estimates of receptor numbers and degradation rate. (A) Normalized fluorescent GFP intensity in *hh-Nb1^{high}CD8* (green bar) and *hh-Gal4, UAS-Nb1^{high}CD8* (orange bar) after *ex vivo* incubation in a 400 nM GFP bath on ice (see methods). The difference in GFP intensity suggests that Gal4-mediated expression leads to a ~20 fold increase in surface receptor levels. **(B)** Nb1^{high}CD8-expressing discs were saturated with GFP on ice, washed, incubated for different durations in Schneider's medium at 25°C, and imaged. Normalized GFP intensity in *hh-Nb1^{high}CD8* wing discs decreased by ~25% over the time course of 6 h. Since GFP is quenched in late endosomes due to a low pH (*58*), this observation suggests that Nb1^{high}CD8 is degraded only slowly (on the scale of several hours as predicted by modelling). **(C)** The same experiment with *hh-Nb1^{high}GPI* wing discs suggests almost no degradation of Nb1^{high}GPI over the time course of 4 h. **(D-F)** To estimate the concentration of Nb1^{high}CD8 at the cell surface, a GFP invasion assay was used. *hh-Nb1^{high}CD8* discs were incubated in 2 nM, 20 nM and 200 nM GFP baths for 5 min at 25°C. The resulting basal-to-apical GFP gradient in the posterior compartment was imaged (D) and quantified (F). A simple model (see (E) and section 1.7 of Supplementary Theory) was used to fit the measured GFP fluorescence profiles (G) and derive the surface density and lateral diffusion constant of binders.

Fig. S8. Engineering receptors that activate Dpp signaling in response to GFP. (A) Dpp dimers normally bring together a pair of type I (Tkv, red) and a pair of type II receptors (Put, blue) to promote phosphorylation (black dots) of the downstream effector Mad. These receptors

were rendered GFP-responsive by inserting anti-GFP nanobodies in the extracellular domain, as previously described for cytokine receptors (*59*). (B) S2 cells became responsive to GFP upon expression of these engineered receptors. S2 cells were transfected with CMV-Nb1^{high}Put, CMV-Nb2^{high}Tkv and tubulin-FLAG:Mad. Thirty six hours later, cells were incubated with mock medium, GFP conditioned medium, GFP dimer conditioned medium or commercially available GFP (5 ng/ml) and protein was extracted for Western blotting. Phosphorylation of Mad was seen within 30 min of adding GFP or GFP dimers in the medium. Syntaxin was used as a loading control. Activation by GFP monomer shows that dimers are not required, indicating some flexibility about the ligand configuration needed for activation (*60*).

Fig. S9. Validation of the *dpp-[>HA:Dpp>SecGFP:GFP]* allele. (A) In wing discs homozygous for *dpp-[>HA:Dpp>SecGFP:GFP]*, HA-tagged Dpp is the sole source of Dpp protein. In the absence of Flp, HA:Dpp is expressed in a stripe of cells along the A/P boundary. (B) Expression of Flp in the wing pouch with *rotund-Gal4* (*rn-Gal4*) (*61*), results in the loss of HA:Dpp and *de novo* GFP expression in the *Dpp*-producing cells. (C, D) In the absence of Flp (same genotype as panel A), Brk forms the same inverse gradient as in wild type discs. Upon Flp expression (same genotype as panel B), Brk is expressed throughout pouch, as expected from removal of Dpp signaling. Scale bars: 50 μm.

Fig. S10. Progressive downregulation of signaling within the source of GFP. (A) Key components of the SR rescue configuration: the ligand, SecGFP:GFP, expressed instead of Dpp and the engineered signaling receptors (SR), expressed under the control of the *ubiquitin* promoter. Under these conditions pMad immunoreactivity is high on either side of the SecGFP:GFP expression domain (as expected), but with an unexpected zone of reduced activity inside the source (Fig. 4D, column 3). (B, C) The band of reduced signaling activity is not due to receptor down-regulation since the profile of V5-tagged Nb2^{high}Tkv (n=5) actually shows a slight upregulation at the anterior side of the boundary. (D-F) pMad immunoreactivity in discs of various stages (same genotype as in Fig. 4D, column 3, SR) shows that the band of pMad reduction develops over time. While pMad immunoreactivity is detected throughout the GFP-expressing domain in early (~74 h after egg laying (AEL)) and mid (~96 h AEL) 3rd instar wing discs, it was markedly decreased in the GFP-producing cells of late 3rd instar wing discs. One possibility is that desensitization results from receptor inactivation in cis by high level of ligand or from depletion of free surface receptors over time. Scale bars: 50 μm.

Fig. S11. Overexpression of low-affinity non-receptors inhibits signaling by GFP. Immunofluorescence analysis (proteins indicated) shows signaling activity in two genotypes. Left column shows a control disc (same genotype as in the first column of Fig. 4). Right column shows a disc lacking Dpp but expressing SecGFP:GFP and the engineered signaling receptors (SR) and also 'over-expressing' Nb^{low}GPI (*rn-Gal4, UAS-Nb^{low}GPI*). By comparison to the positive control and SR only rescue (Fig. 4, column 3, no *UAS-Nb^{low}GPI*), pMad is strongly decreased. Moreover, Brk is somewhat derepressed, the expression domain of Omb is narrow,

Sal is nearly absent from the posterior compartment, and DSRF immunoreactivity does not reveal distinguishable proveins L2 and L5. As expected then, the resulting wings are poorly patterned. Scale bar wing discs: 50 μm. Scale bar adult wings: 0.25 mm.

Fig. S12. Addition of GPI-anchored non-signaling receptors reduces wing size variation. Genotypes (only males) are indicated. Mean and standard derivation are shown. Coefficient of variation as follows: positive control: 2.76%; negative control: 15.63%; SR: 9.38%; SR+NR: 3.56%; SR+ SR: N/A (n too small). Wings rescued by SR were more variable in size than wild type wings and this was partially rescued by addition of NR expressed from the *dally* locus.

Fig. S13. Role of hopping and handover of the non-signaling receptor. (A) Diffusion-leakage-degradation models with one or two receptor types, as discussed in Supplementary Theory: (a) simple model of ligand binding to immobile, membrane-bound receptors. (b) As in (a), but with receptor release from the membrane and subsequent reinsertion. (c) As in (a) but considering effective diffusion of receptors at the surface of the tissue, through membrane diffusion and hopping. (d) As in (c), but with two receptor types: one type of receptor is allowed to hop and diffuse, while the second type remains membrane-bound and immobile. The two receptor types are color-coded according to the convention for SR/NR followed in Fig. 5. **(B)** Signaling activity profile predicted by the simplified model of panel A(d) in the three experimental conditions of interest, namely SR (blue), SR+SR (green), SR+NR (red). These gradients are qualitatively similar to those shown in Fig. 5B. See Supplementary Theory for parameters. **(C)** Schematic of the reactions involved in the two-receptor model with GFP dimer (as in Fig. 5A). The arrows indicate reversible transitions and have been labelled according to the notation introduced in Supplementary Theory. The colored boxes contain subgraphs corresponding to the different mechanisms at play in the model, namely single and double binding to receptors (red), handover (orange), hopping (blue). **(D)** Concentration gradient of signaling complex obtained from the two-receptor model with GFP dimer shown in (C), for different choices of effective NR diffusion coefficient D_{r}. Introducing a non-diffusing NR (orange curve) shortens the gradient compared to the case with SR only (blue curve). In line with our analytical calculations, the gradient length scale is however observed to increase with increasing NR diffusion constant D_{r}. The dotted line indicates 1/e of the maximal value of the SR only profile, used to determine gradient extension factors in panel (E). Other parameters are as described in Supplementary Theory. **(E)** Blue line: Gradient extension factor as a function of the effective NR diffusion coefficient D_{r} (other parameters are as described in Supplementary theory), in the simplified model with two receptors (panel A (d)), in the regime far from receptor saturation (see section 2.1.3 in Supplementary Theory for details). The gradient extension factor is defined as the ratio of the longer gradient length scale for a given value of D_{r} and for $D_{\mathrm{r}} = 0$, with other parameters kept the same. The dashed line indicates no extension of the gradients, and its intersection with the blue line sets the threshold diffusion coefficient D_r^* for gradient extension. Square marks: gradient extension factor obtained with characteristic length scales extracted from the curves in Panel (D), plotted for comparison with the result of the simplified model.

4. SUPPLEMENTARY TABLES

	GFP/pMad gradient length scale (distance to 50% max. intensity)	**Non-zero tail** (relative to max. intensity)
Figure 1D		
hh-Nb1^{high}CD8	30.1 ± 2.0 µm	35.0 ± 4.0 %
hh-Nb1^{high}CD8 + fat body trap	18.3 ± 2.5 µm	6.4 ± 1.6 %
hh-Nb^{low}CD8	n/a	77.2 ± 5.8%
Figure 3C		
hh-Gal4, UAS- Nb1^{high}CD8	4.7 ± 0.6 µm	4.8 ± 1.6 %
Figure 4D		
Positive control	11.6 ± 2.5 µm	2.6 ± 0.8 %
SR	9.0 ± 1.2 µm	25.2 ± 4.3 %
SR+SR	2.8 ± 1.4 µm	4.8 ± 2.1 %
SR+NR	29.7 ± 4.1 µm	6.4 ± 5.0 %

Table S1: Length scales (distance where the gradient falls to 50% of its maximal intensity) and non-zero tail values (fluorescence intensity relative to the maximal intensity) of GFP (Fig. 1D and 3C) and pMad (Fig. 4D) gradients in the posterior wing disc compartment.

Parameter	Name	Value	Unit	
Free ligand diffusion constant	D	21	$\mu m^2.s^{-1}$	As measured for Dpp (*2*)
Thickness of intercellular space	h	20	nm	Estimated from EM
Tissue height	H	53	µm	Measured (n=10 wing discs)
Length of one AP compartment	L	116	µm	Measured (n=10 wing discs)
Length of the source	L_S	26	µm	Measured (n=11 wing discs)
Binding rate of GFP to Nb^{high} (GBP1)	$k_{on}^{Nb^{high}}$	7.7×10^{-4}	$nM^{-1}.s^{-1}$	(*15, 34*)
Unbinding rate of GFP from Nb^{high} (GBP1)	$k_{off}^{Nb^{high}}$	1.7×10^{-4}	s^{-1}	(*15, 34*)
Binding rate of GFP to Nb^{low} (LAG3)	$k_{on}^{Nb^{low}}$	2×10^{-3}	$nM^{-1}.s^{-1}$	(*17*)
Unbinding rate of GFP from Nb^{low} (LAG3)	$k_{off}^{Nb^{low}}$	5×10^{-2}	s^{-1}	(*17*)
Ligand production rate in the source	j	0.3	$nM.s^{-1}$	Fitted
Leakage rate to hemolymph	κ	0.075	s^{-1}	Fitted
Rescaled degradation rate in hemolymph	$\bar{k}_H$	0.01	s^{-1}	Fitted
Rescaled degradation rate in hemolymph, fat body experiment	$\bar{k}_H^{FB}$	0.19	s^{-1}	Fitted
Receptor production rate	j_r	0.0026	$nM.\mu m.s^{-1}$	Fitted

Table S2. Parameters for the single receptor model (EM = electron microscopy).

Parameter	Name	Value	Unit	
GFP dimer diffusion constant	D	$21 \times 2^{-\frac{1}{3}}$	$\mu m^2.s^{-1}$	Estimated from D in Table S2
Effective NR diffusion constant	D_r	0.1	$\mu m^2.s^{-1}$	(*47, 48*)
Degradation rate signaling configuration	k^{aa}	2.1×10^{-3}	s^{-1}	(*2*)
Degradation rate non-signaling configuration	k^a, k^b, k^{bb}, k^{ab}	2.6×10^{-5}	s^{-1}	from j^r by fixing $n_T = 100$ nM. µm
SR production rate	j_r^a	2.6×10^{-3}	nM. µm. s^{-1}	as in Table S2
NR production rate	j_r^b	2.6×10^{-3}	nM. µm. s^{-1}	as in Table S2

Table S3: Parameters for the numerical simulations of the two-receptor models. Unlisted parameters are as in Table S2 or given in the Supplementary Theory text.

5. SUPPLEMENTARY REFERENCES

34. M. H. Kubala, O. Kovtun, K. Alexandrov, B. M. Collins, Structural and thermodynamic analysis of the GFP:GFP-nanobody complex. *Protein Sci.* **19**, 2389-2401 (2010).
35. A. Kicheva *et al.*, Kinetics of morphogen gradient formation. *Science* **315**, 521-525 (2007).
36. F. Zhang *et al.*, Quantification of epidermal growth factor receptor expression level and binding kinetics on cell surfaces by surface plasmon resonance imaging. *Anal. Chem.* **87**, 9960-9965 (2015).
37. T. Tabata, S. Eaton, T. B. Kornberg, The Drosophila hedgehog gene is expressed specifically in posterior compartment cells and is a target of engrailed regulation. *Genes & Development* **6**, 2635-2645 (1992).
38. J. J. Lee, D. P. von Kessler, S. Parks, P. A. Beachy, Secretion and localized transcription suggest a role in positional signaling for products of the segmentation gene hedgehog. *Cell* **71**, 33-50 (1992).
39. J. E. Hooper, Smoothened translates Hedgehog levels into distinct responses. *Development (Cambridge, England)* **130**, 3951-3963 (2003).
40. B. Glise, D. L. Jones, P. W. Ingham, Notch and Wingless modulate the response of cells to Hedgehog signalling in the Drosophila wing. *Dev. Biol.* **248**, 93-106 (2002).
41. A. Kopp, I. Duncan, Anteroposterior patterning in adult abdominal segments of Drosophila. *Dev. Biol.* **242**, 15-30 (2002).
42. C. Zihni, C. Mills, K. Matter, M. S. Balda, Tight junctions: from simple barriers to multifunctional molecular gates. *Nat. Rev. Mol. Cell Biol.* **17**, 564-580 (2016).
43. L. Hufnagel, J. Kreuger, S. M. Cohen, B. I. Shraiman, On the role of glypicans in the process of morphogen gradient formation. *Dev. Biol.* **300**, 512-522 (2006).
44. T. Kirsch, W. Sebald, M. K. Dreyer, Crystal structure of the BMP-2-BRIA ectodomain complex. *Nat. Struct. Biol.* **7**, 492-496 (2000).
45. J. Thurmond *et al.*, FlyBase 2.0: the next generation. *Nucleic Acids Res.* **47**, D759-D765 (2019).
46. B. R. Graveley *et al.*, The developmental transcriptome of Drosophila melanogaster. *Nature* **471**, 473-479 (2011).
47. S. Saha, A. A. Anilkumar, S. Mayor, GPI-anchored protein organization and dynamics at the cell surface. *J. Lipid Res.* **57**, 159-175 (2016).
48. S. Wieser, M. Moertelmaier, E. Fuertbauer, H. Stockinger, G. J. Schutz, (Un)confined diffusion of CD59 in the plasma membrane determined by high-resolution single molecule microscopy. *Biophys. J.* **92**, 3719-3728 (2007).
49. L. A. Baena-López, C. Alexandre, A. Mitchell, L. Pasakarnis, J.-P. Vincent, Accelerated homologous recombination and subsequent genome modification in Drosophila. *Development* **140**, 4818-4825 (2013).
50. R. Yagi, F. Mayer, K. Basler, Refined LexA transactivators and their use in combination with the Drosophila Gal4 system. *Proc. Natl. Acad. Sci. U. S. A.* **107**, 16166-16171 (2010).
51. M. Brankatschk, S. Eaton, Lipoprotein particles cross the blood-brain barrier in Drosophila. *J. Neurosci.* **30**, 10441-10447 (2010).
52. S. Pfeiffer, C. Alexandre, M. Calleja, J. P. Vincent, The progeny of wingless-expressing cells deliver the signal at a distance in Drosophila embryos. *Curr. Biol.* **10**, 321-324 (2000).

53. I. J. McGough *et al.*, Glypicans shield the Wnt lipid moiety to enable signalling at a distance. *Nature* **in press**, (2020).
54. S. J. Gratz *et al.*, Genome engineering of Drosophila with the CRISPR RNA-guided Cas9 nuclease. *Genetics* **194**, 1029-1035 (2013).
55. Z. Liu *et al.*, Systematic comparison of 2A peptides for cloning multi-genes in a polycistronic vector. *Sci. Rep.* **7**, 2193 (2017).
56. J. Shen, C. Dahmann, G. O. Pflugfelder, Spatial discontinuity of optomotor-blind expression in the Drosophila wing imaginal disc disrupts epithelial architecture and promotes cell sorting. *BMC Dev. Biol.* **10**, 23 (2010).
57. J. Schindelin *et al.*, Fiji: an open-source platform for biological-image analysis. *Nat. Methods* **9**, 676-682 (2012).
58. L. Couturier, M. Trylinski, K. Mazouni, L. Darnet, F. Schweisguth, A fluorescent tagging approach in Drosophila reveals late endosomal trafficking of Notch and Sanpodo. *The Journal of cell biology* **207**, 351-363 (2014).
59. E. Engelowski *et al.*, Synthetic cytokine receptors transmit biological signals using artificial ligands. *Nat. Commun.* **9**, 2034 (2018).
60. T. Huang *et al.*, TGF-beta signalling is mediated by two autonomously functioning TbetaRI:TbetaRII pairs. *EMBO J.* **30**, 1263-1276 (2011).
61. S. E. St Pierre, M. I. Galindo, J. P. Couso, S. Thor, Control of Drosophila imaginal disc development by rotund and roughened eye: differentially expressed transcripts of the same gene encoding functionally distinct zinc finger proteins. *Development* **129**, 1273-1281 (2002).

Figure S1

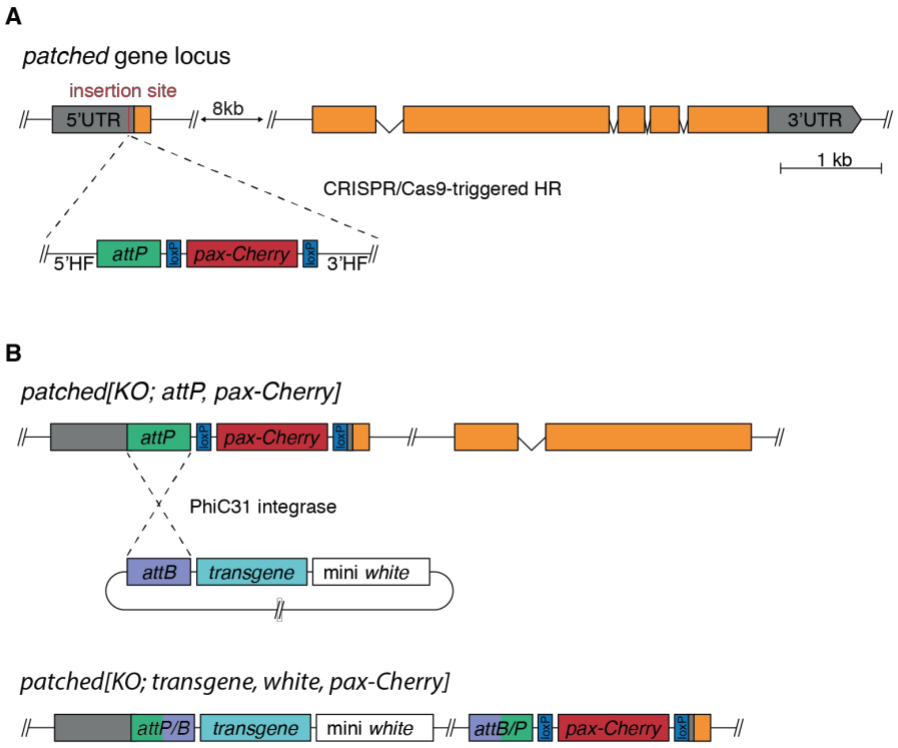
A
patched gene locus
insertion site
5'UTR
8kb
3'UTR
1 kb
CRISPR/Cas9-triggered HR
5'HF
attP
loxP
pax-Cherry
loxP
3'HF
B
patched[KO; attP, pax-Cherry]
attP
loxP
pax-Cherry
loxP
PhiC31 integrase
attB
transgene
mini white
patched[KO; transgene, white, pax-Cherry]
attP/B
transgene
mini white
attB/P
loxP
pax-Cherry
loxP

5

Figure S2

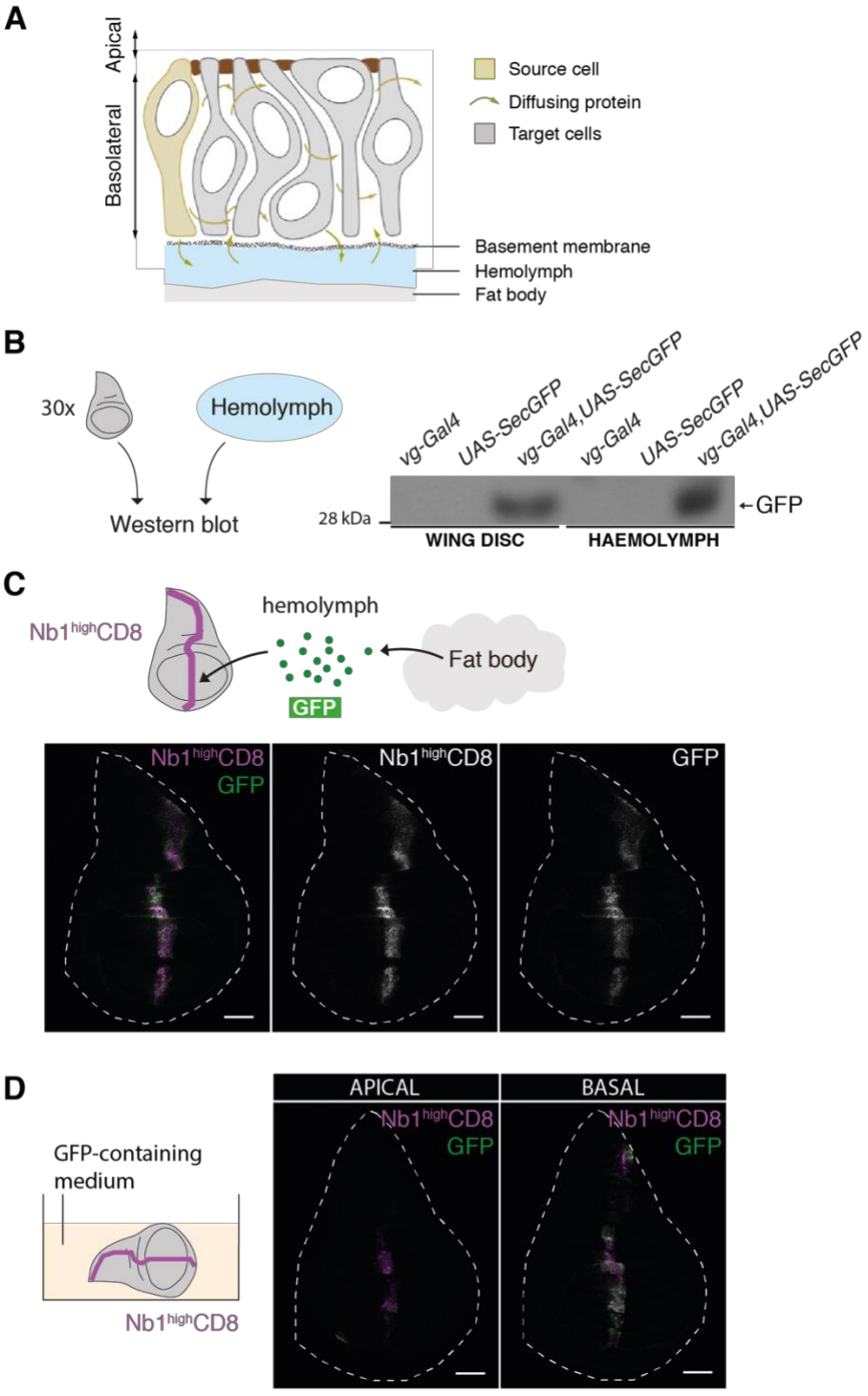
A
Apical
Basolateral
Source cell
Diffusing protein
Target cells
Basement membrane
Hemolymph
Fat body
B
30x
Hemolymph
Western blot
vg-Gal4
UAS-SecGFP
vg-Gal4,UAS-SecGFP
vg-Gal4
UAS-SecGFP
vg-Gal4,UAS-SecGFP
28 kDa
←GFP
WING DISC
HAEMOLYMPH
C
Nb1highCD8
hemolymph
Fat body
GFP
Nb1highCD8
GFP
Nb1highCD8
GFP
D
GFP-containing medium
Nb1highCD8
APICAL
BASAL
Nb1highCD8
GFP
Nb1highCD8
GFP

5

Figure S3

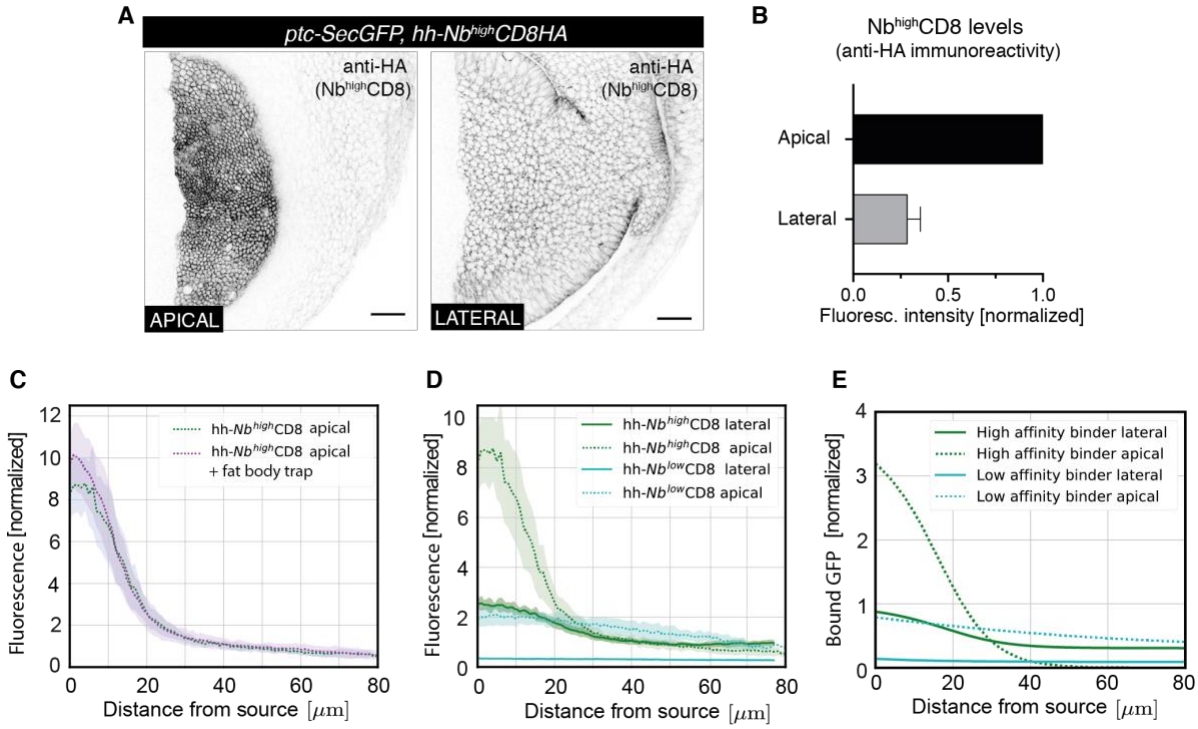
A
ptc-SecGFP, hh-Nb^highCD8HA
anti-HA (Nb^highCD8)
APICAL
anti-HA (Nb^highCD8)
LATERAL
B
Nb^highCD8 levels
(anti-HA immunoreactivity)
Apical
Lateral
0.0
0.5
1.0
Fluoresc. intensity [normalized]
C
Fluorescence [normalized]
hh-Nb^highCD8 apical
hh-Nb^highCD8 apical + fat body trap
Distance from source [μm]
D
Fluorescence [normalized]
hh-Nb^highCD8 lateral
hh-Nb^highCD8 apical
hh-Nb^lowCD8 lateral
hh-Nb^lowCD8 apical
Distance from source [μm]
E
Bound GFP [normalized]
High affinity binder lateral
High affinity binder apical
Low affinity binder lateral
Low affinity binder apical
Distance from source [μm]

5

Figure S4

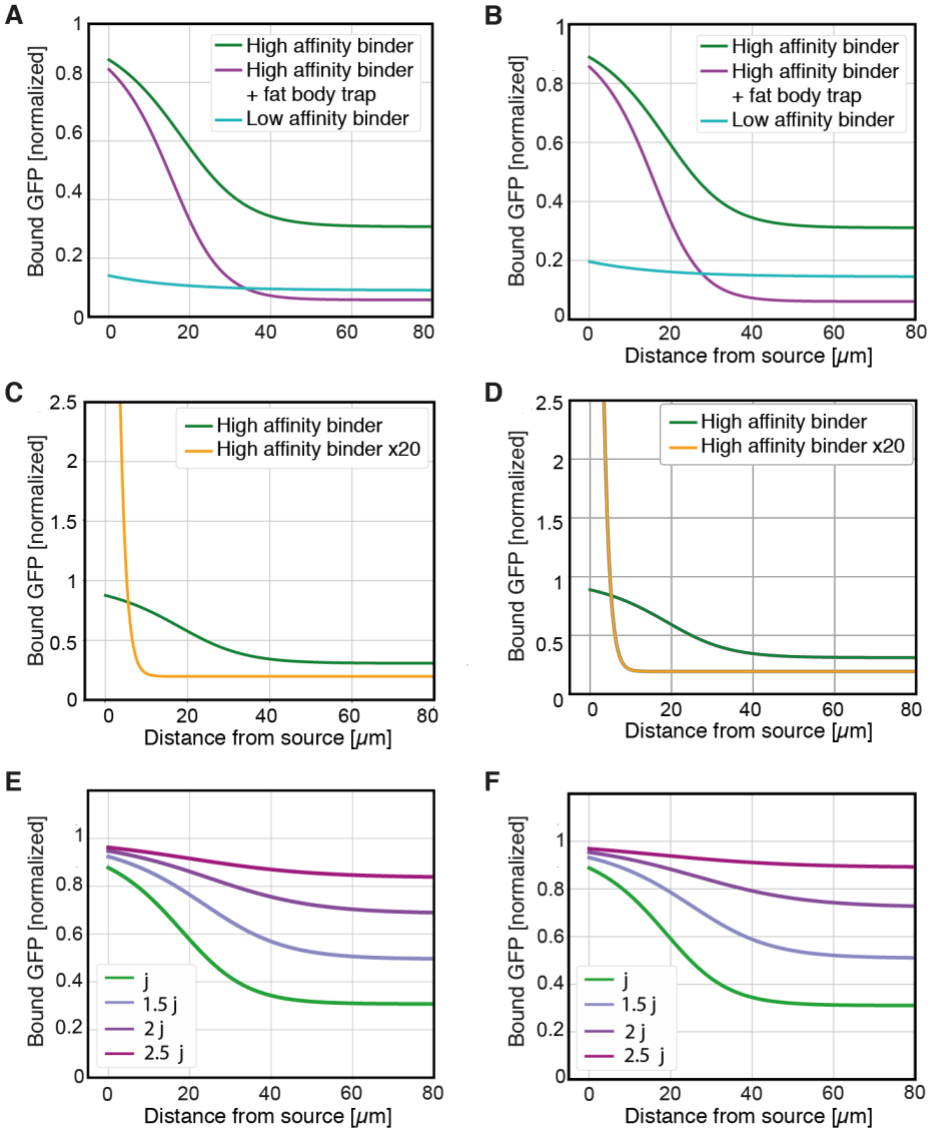
A
B
C
D
E
F
Bound GFP [normalized]
Distance from source [μm]
High affinity binder
High affinity binder + fat body trap
Low affinity binder
High affinity binder x20
j
1.5 j
2 j
2.5 j

5

Figure S5

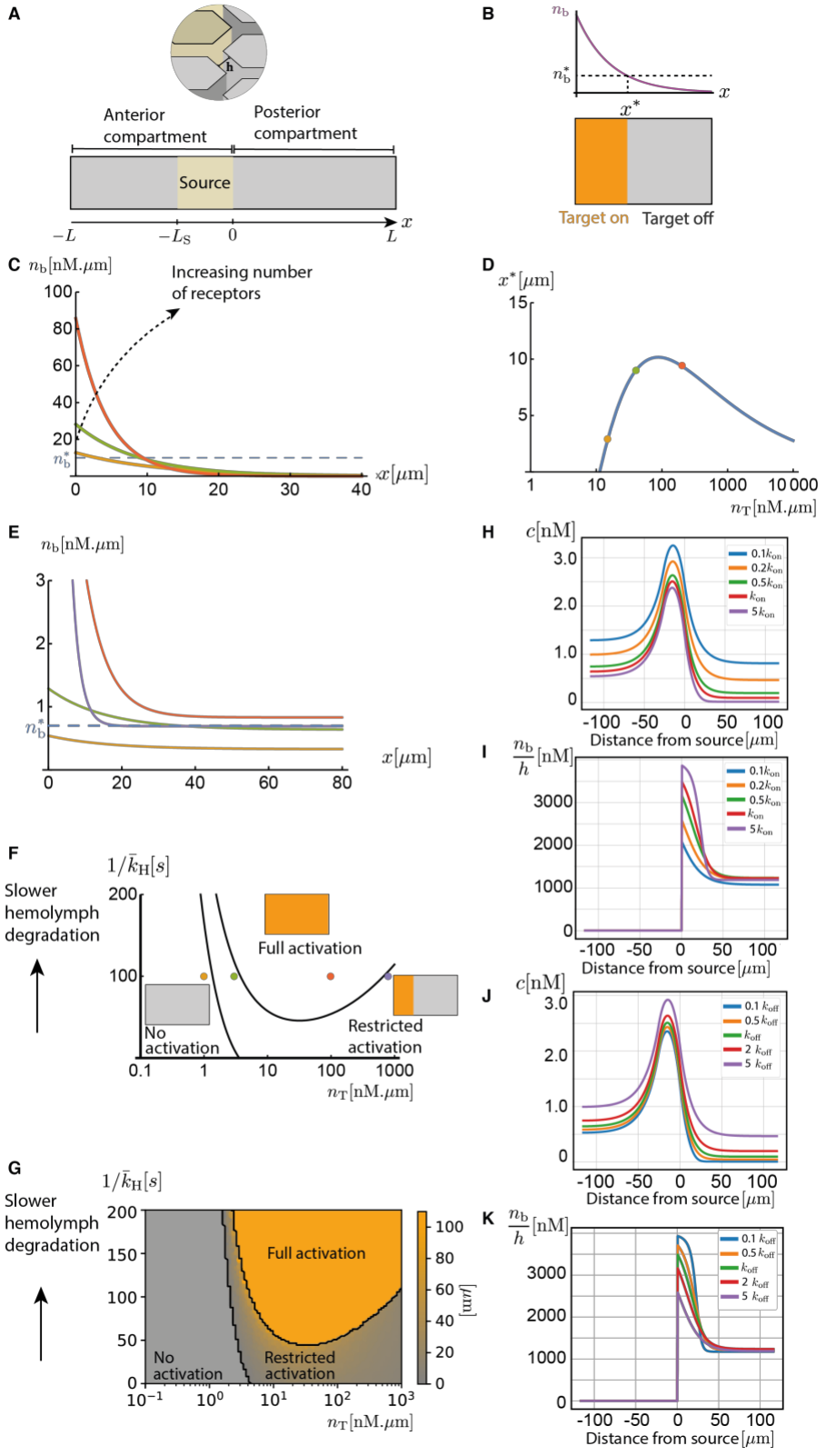
A
h
Anterior compartment
Posterior compartment
Source
$-L$
$-L_S$
0
L
x
B
n_b
n_b^*
x
x^*
Target on
Target off
C
n_b[nM.μm]
Increasing number of receptors
100
80
60
40
20
n_b^*
0
10
20
30
40
$x[\mu m]$
D
$x^*[\mu m]$
15
10
5
1
10
100
1000
10 000
n_T[nM.μm]
E
n_b[nM.μm]
3
2
1
n_b^*
0
20
40
60
80
$x[\mu m]$
F
$1/\bar{k}_H[s]$
Slower hemolymph degradation
200
100
Full activation
No activation
Restricted activation
0.1
1
10
100
1000
n_T[nM.μm]
G
$1/\bar{k}_H[s]$
Slower hemolymph degradation
200
150
100
50
0
Full activation
No activation
Restricted activation
10^{-1}
10^0
10^1
10^2
10^3
n_T[nM.μm]
100
80
60
40
20
0
[nM]
H
c[nM]
3.0
2.0
1.0
0
$0.1k_{on}$
$0.2k_{on}$
$0.5k_{on}$
k_{on}
$5k_{on}$
-100 -50 0 50 100
Distance from source[μm]
I
$\frac{n_b}{h}$[nM]
3000
2000
1000
0
$0.1k_{on}$
$0.2k_{on}$
$0.5k_{on}$
k_{on}
$5k_{on}$
-100 -50 0 50 100
Distance from source[μm]
J
c[nM]
3.0
2.0
1.0
0
$0.1\ k_{off}$
$0.5\ k_{off}$
k_{off}
$2\ k_{off}$
$5\ k_{off}$
-100 -50 0 50 100
Distance from source[μm]
K
$\frac{n_b}{h}$[nM]
3000
2000
1000
0
$0.1\ k_{off}$
$0.5\ k_{off}$
k_{off}
$2\ k_{off}$
$5\ k_{off}$
-100 -50 0 50 100
Distance from source[μm]

Figure S6

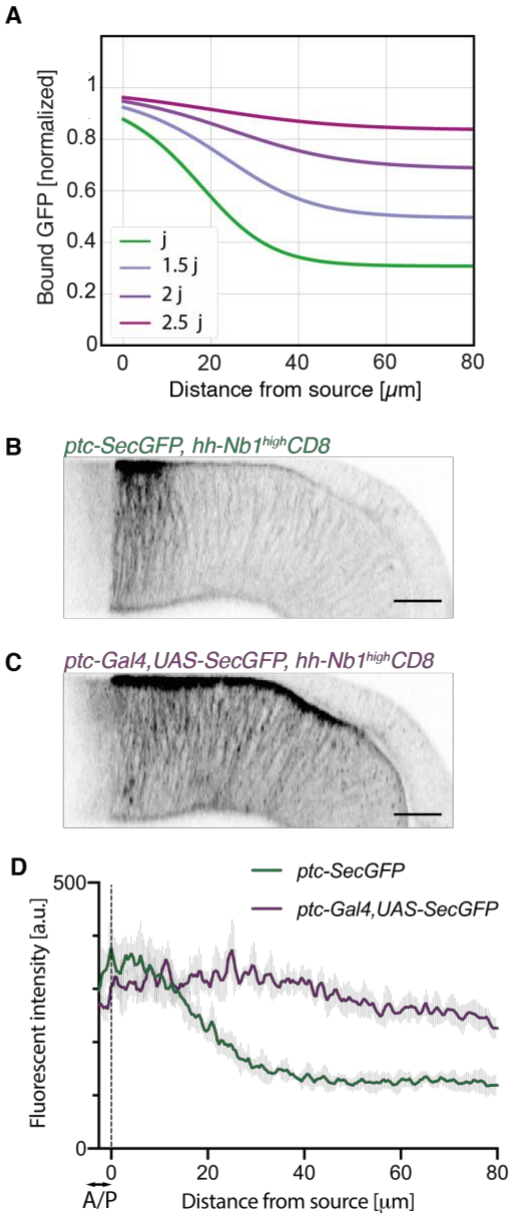
A
Bound GFP [normalized]
1
0.8
0.6
0.4
0.2
0
j
1.5 j
2 j
2.5 j
0
20
40
60
80
Distance from source [μm]
B
ptc-SecGFP, hh-Nb1highCD8
C
ptc-Gal4,UAS-SecGFP, hh-Nb1highCD8
D
ptc-SecGFP
ptc-Gal4,UAS-SecGFP
Fluorescent intensity [a.u.]
500
0
0
20
40
60
80
A/P
Distance from source [μm]

5

Figure S7

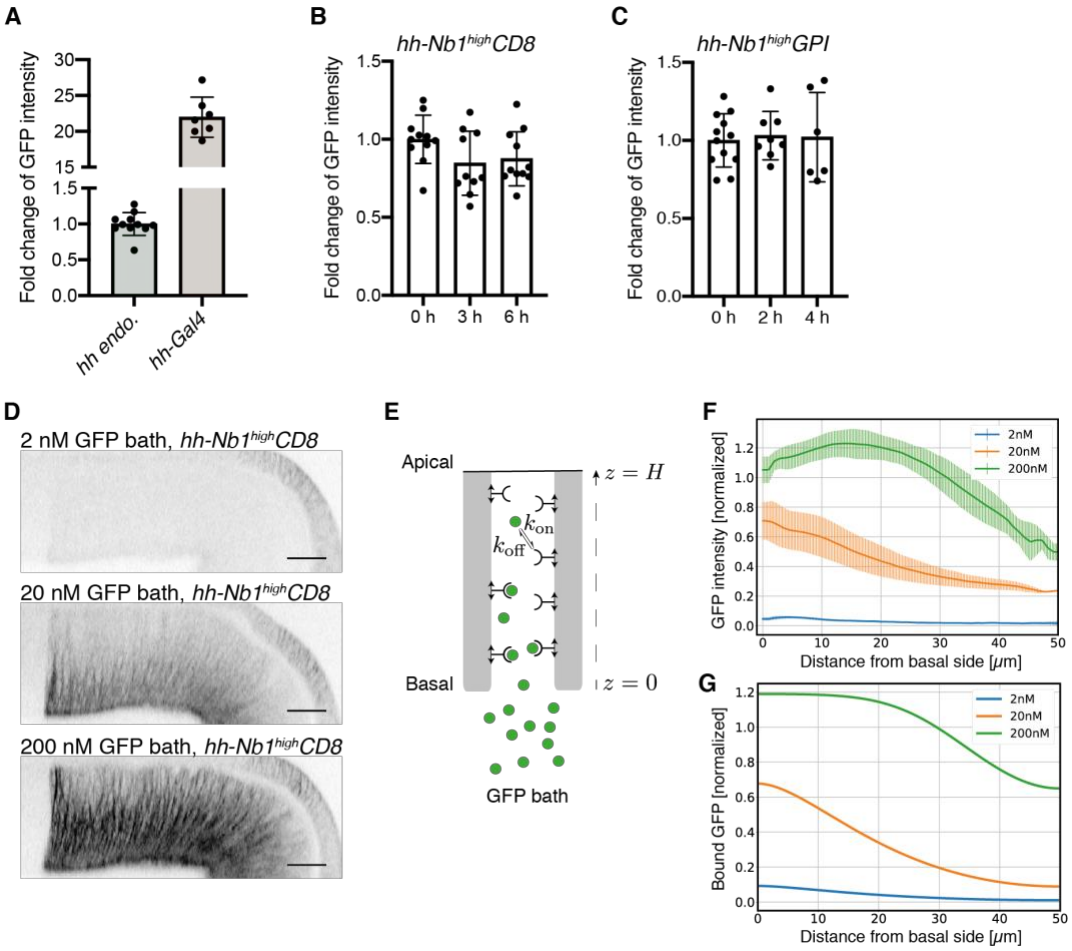
A
Fold change of GFP intensity
hh endo.
hh-Gal4
B
hh-Nb1highCD8
Fold change of GFP intensity
0 h
3 h
6 h
C
hh-Nb1highGPI
Fold change of GFP intensity
0 h
2 h
4 h
D
2 nM GFP bath, hh-Nb1highCD8
20 nM GFP bath, hh-Nb1highCD8
200 nM GFP bath, hh-Nb1highCD8
E
Apical
Basal
GFP bath
F
GFP intensity [normalized]
Distance from basal side [μm]
2nM
20nM
200nM
G
Bound GFP [normalized]
Distance from basal side [μm]

Figure S8

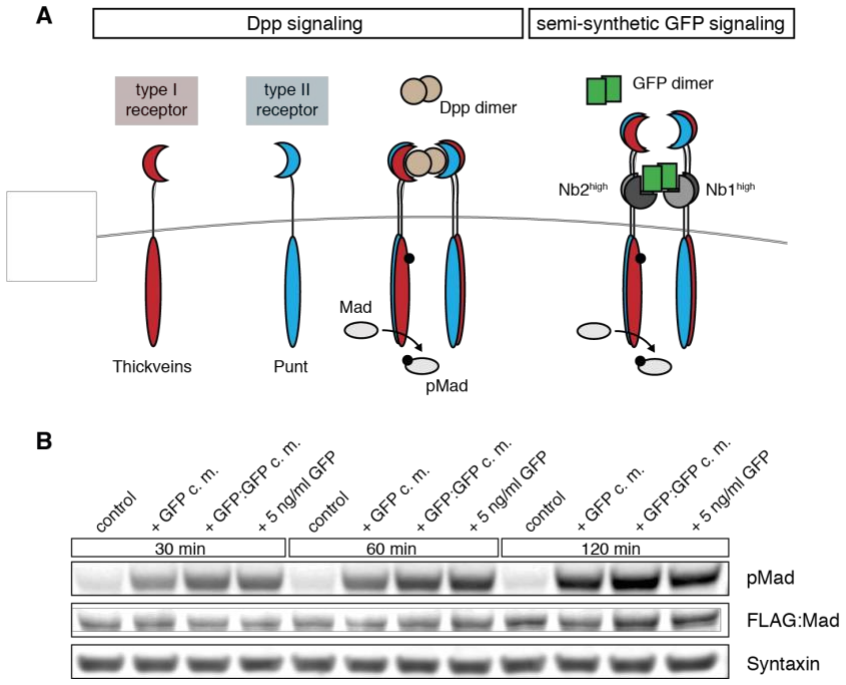
A
Dpp signaling
semi-synthetic GFP signaling
type I receptor
type II receptor
Dpp dimer
GFP dimer
Nb2high
Nb1high
Mad
Thickveins
Punt
pMad
B
control
+ GFP c. m.
+ GFP:GFP c. m.
+ 5 ng/ml GFP
30 min
60 min
120 min
pMad
FLAG:Mad
Syntaxin

5

Figure S9

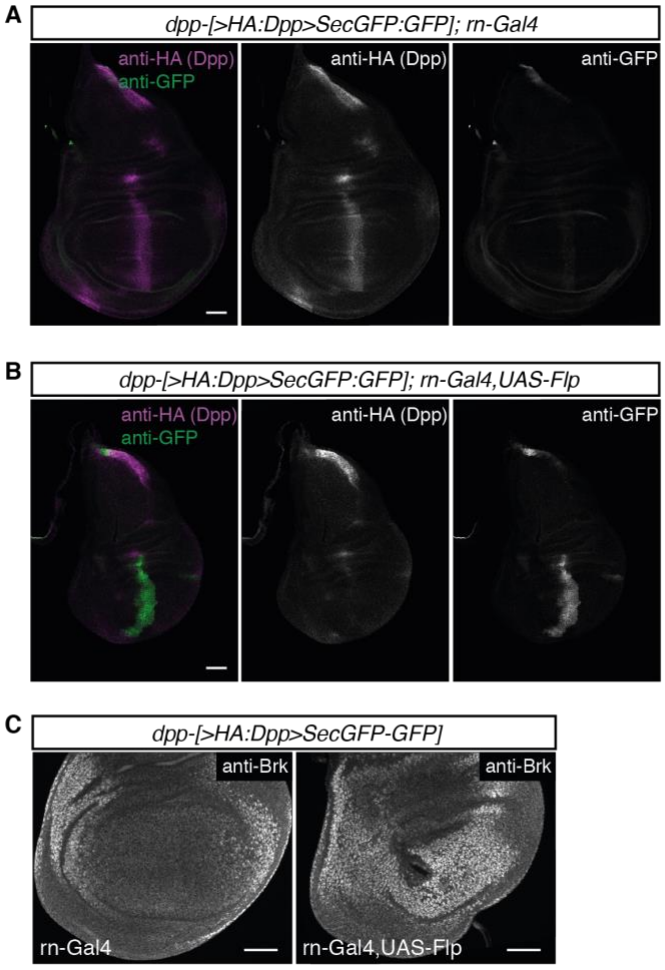
A
dpp-[>HA:Dpp>SecGFP:GFP]; rn-Gal4
anti-HA (Dpp)
anti-GFP
anti-HA (Dpp)
anti-GFP
B
dpp-[>HA:Dpp>SecGFP:GFP]; rn-Gal4,UAS-Flp
anti-HA (Dpp)
anti-GFP
anti-HA (Dpp)
anti-GFP
C
dpp-[>HA:Dpp>SecGFP-GFP]
anti-Brk
anti-Brk
rn-Gal4
rn-Gal4,UAS-Flp

5

Figure S10

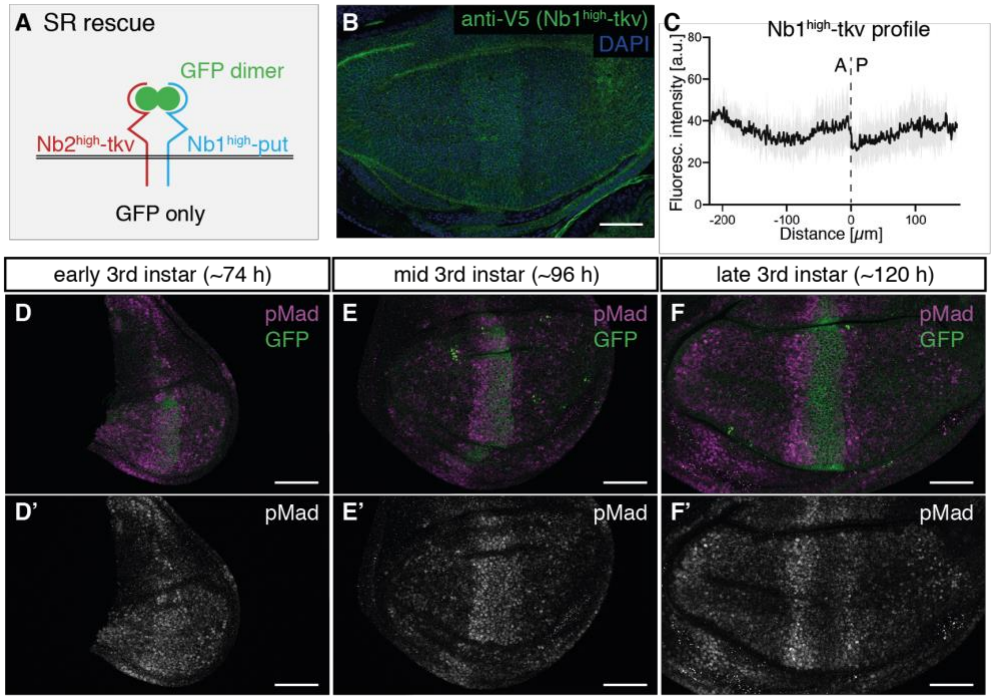
A SR rescue
GFP dimer
Nb2high-tkv
Nb1high-put
GFP only
B
anti-V5 (Nb1high-tkv)
DAPI
C
Nb1high-tkv profile
A
P
Fluoresc. intensity [a.u.]
Distance [μm]
early 3rd instar (~74 h)
mid 3rd instar (~96 h)
late 3rd instar (~120 h)
D
E
F
pMad
GFP
D'
E'
F'
pMad

5

Figure S11

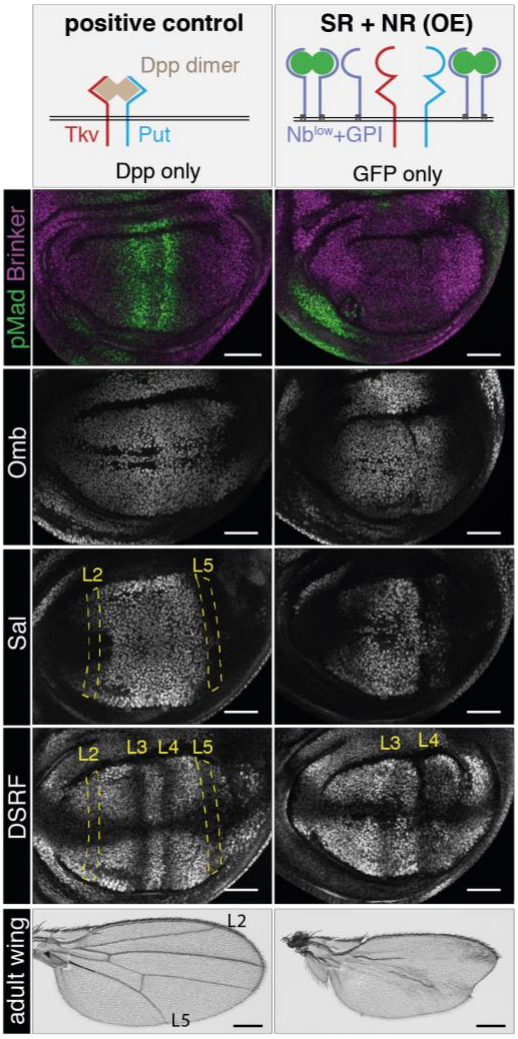
positive control
SR + NR (OE)
Dpp dimer
Tkv
Put
Nb^low+GPI
Dpp only
GFP only
pMad Brinker
Omb
Sal
L2
L5
DSRF
L2
L3
L4
L5
L3
L4
adult wing
L2
L5

5

Figure S12

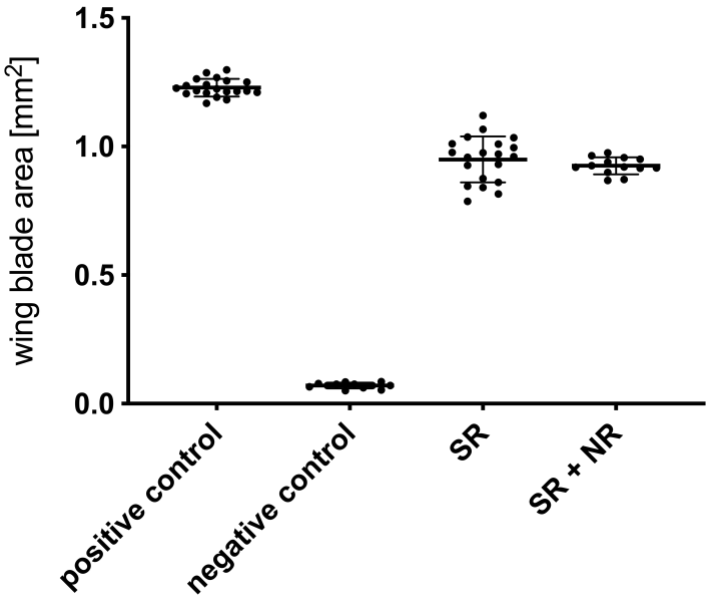
wing blade area [mm²]
1.5
1.0
0.5
0.0
positive control
negative control
SR
SR + NR

5

Figure S13

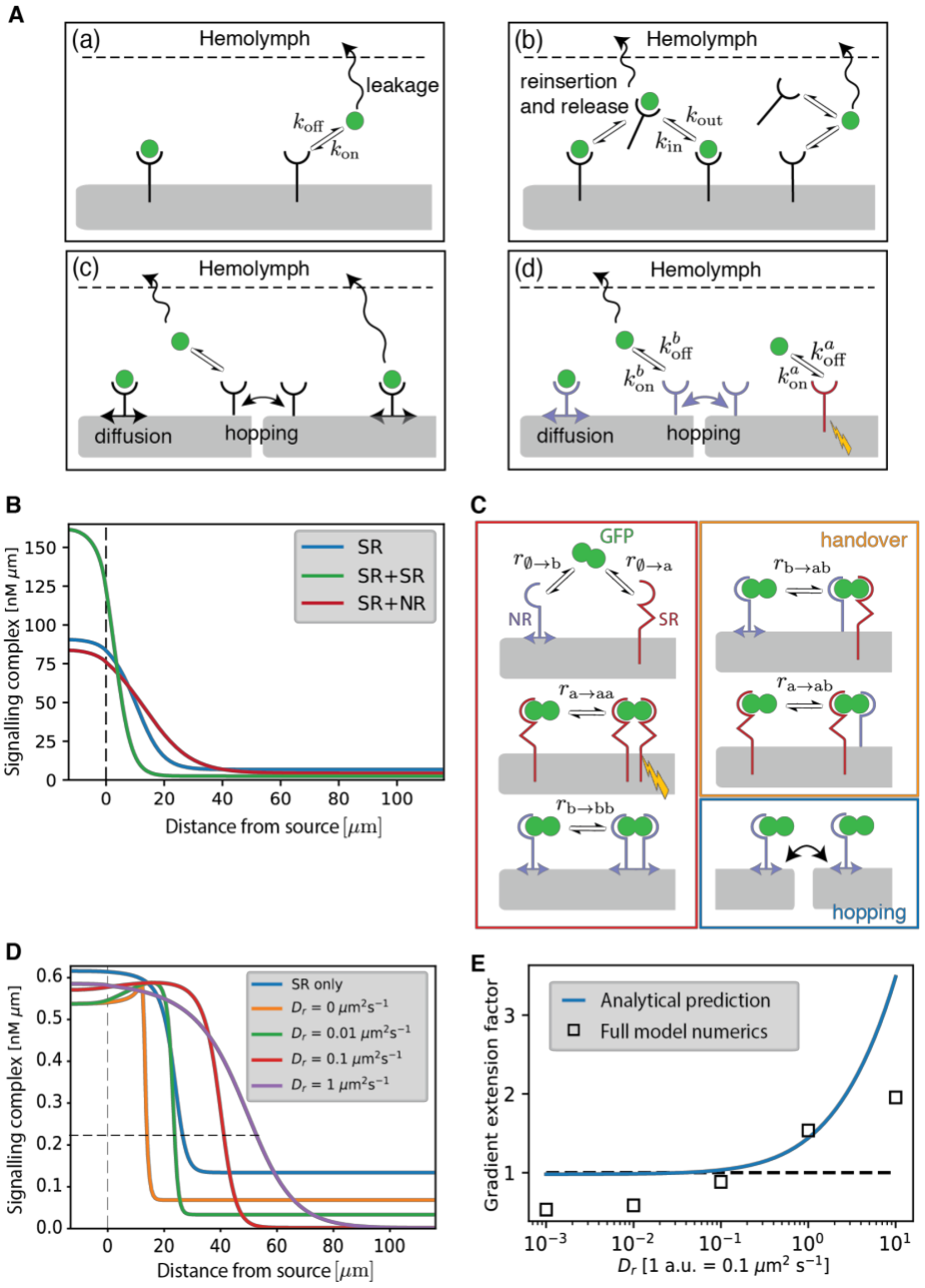
A
(a)
Hemolymph
leakage
k_{off}
k_{on}
(b)
Hemolymph
reinsertion
and release
k_{out}
k_{in}
(c)
Hemolymph
diffusion
hopping
(d)
Hemolymph
k^b_{off}
k^b_{on}
k^a_{off}
k^a_{on}
diffusion
hopping
B
Signalling complex [nM μm]
SR
SR+SR
SR+NR
Distance from source [μm]
C
GFP
$r_{\emptyset\to b}$
$r_{\emptyset\to a}$
NR
SR
$r_{a\to aa}$
$r_{b\to bb}$
handover
$r_{b\to ab}$
$r_{a\to ab}$
hopping
D
Signalling complex [nM μm]
SR only
D_r = 0 $\mu m^2 s^{-1}$
D_r = 0.01 $\mu m^2 s^{-1}$
D_r = 0.1 $\mu m^2 s^{-1}$
D_r = 1 $\mu m^2 s^{-1}$
Distance from source [μm]
E
Gradient extension factor
Analytical prediction
Full model numerics
D_r [1 a.u. = 0.1 μm^2 s^{-1}]